JOURNAL OF SPACECRAFT AND ROCKETS
Vol. 57, No. 3, May–June 2020

Multiobjective Optimization and Particle-In-Cell Simulation of Cusped Field Thrusters for Microsatellite Platforms

Suk H. Yeo*
RMIT University, Melbourne, Victoria 3001, Australia
Hideaki Ogawa†
Kyushu University, Fukuoka 819-0395, Japan
and
Paul Matthias,‡ Daniel Kahnfeld,‡ and Ralf Schneider§
University of Greifswald, 17498 Greifswald, Germany

https://doi.org/10.2514/1.A34584

A multiobjective design optimization (MDO) study has been conducted to characterize and maximize the performance of the downscaled cusped field thruster with respect to thrust, total efficiency, and specific impulse characterized by common design parameters: anode voltage, anode current, mass flow rate, and geometric configuration. Particle-in-cell (PIC) simulations have been performed for the selected design points identified in MDO study for verification by accurately accounting for phenomena and performance losses that originate from uncertainties and complexities associated with the thruster design and physics. The fidelity of the models employed in MDO has been enhanced owing to the new physical insights gained from the detailed analysis of the PIC results. The prediction errors associated with uncertainties such as the beam current and divergence angle have been reduced to within 5%.

Nomenclature

B	=	magnetic field density, T
B_m	=	magnetic field density at high region, T
B_0	=	magnetic field density at low region, T
F_z	=	axial Lorentz force, N
I_a	=	anode current, A
I_b	=	beam current, A
I_{sp}	=	specific impulse, s
I^+	=	singly charged ion current, A
I^{++}	=	doubly charged ion current, A
K	=	kinetic energy, J
Q	=	average ionic charge, C
q	=	elementary charge, C
m	=	particle mass, kg
$\dot{m}$	=	mass flow rate, standard cm^3/min
$\dot{m}_a$	=	anode mass flow rate, standard cm^3/min
$\dot{m}_i$	=	ionized mass flow rate, standard cm^3/min
N	=	population size
P	=	power, W
P_a	=	anode power, W
P_c	=	cusp arrival probabilities
P_{in}	=	total input power, W
S_i	=	first-order sensitivity index
S_{T_i}	=	total-effect sensitivity index
T	=	thrust, mN
U_a	=	anode potential, V
U_b	=	beam potential, V
ν	=	velocity, m/s
$\nu_\perp$	=	perpendicular velocity of particle, m/s
$\nu_\parallel$	=	parallel velocity of particle, m/s
α_m	=	correction factor
γ	=	plume divergence ratio
η_a	=	anode efficiency, %
η_{acc}	=	acceleration efficiency, %
η_b	=	beam efficiency, %
η_{div}	=	divergence efficiency, %
η_m	=	mass utilization efficiency, %
η_t	=	total efficiency, %
η_ν	=	voltage efficiency, %
θ_{eff}	=	plume divergence angle, °
θ_m	=	pitch angle, deg
μ	=	magnetic moment, J/T

Presented as Paper 2019-1245 at the AIAA Scitech 2019 Forum, San Diego, CA, January 7–11, 2019; received 5 July 2019; revision received 29 December 2019; accepted for publication 31 January 2020; published online 28 February 2020.

*Ph.D. Candidate, Aerospace Engineering and Aviation, School of Engineering. Student Member AIAA.
†Associate Professor, Department of Aeronautics and Astronautics, Graduate School of Engineering. Member AIAA.
‡Ph.D. Student, Institute of Physics.
§Professor of Computational Science and Director of Computing Centre, Institute of Physics.

I. Introduction

IN-SPACE electric propulsion (EP) technologies have been developed over many years for space missions due to their longer operational lifetime, better fuel efficiency, and light weight [1]. They have been used for station keeping for numerous satellites in orbit, and a few have been used for primary propulsion in deep-space scientific missions [1].

In general, EP uses electricity to increase the propellant exhaust velocity, aiming to achieve thrust with high exhaust velocities [1]. The gridded ion thruster and the Hall effect thruster (HET) are well understood and known as the most efficient propulsion types of EP [1]. These classes of propulsion systems offer lifetimes of over 10,000 h and higher specific impulses I_{sp} of 1600–6000 s, but typically lower thrust values of around 30–230 mN [2,3] as compared to chemical propulsion systems. The cusped field thruster (CFT) and a similar thruster design known as the high-efficiency multistage plasma thruster (HEMP-T) have been contrived as a possible concept for future missions to avoid undesirable effects such as wall erosion in a discharging channel while keeping performance at a similar level to that of existing types of EP [2–4].

The HEMP-T was first developed by Thales Electron Devices in 1999, and the CFT was developed by the Harbin Institute of Technology [4,5]. These technologies are based on the principle of electron ionization from the anode and ion acceleration in an electric field, similar to the HET schematically shown in Fig. 1 [6]. A series of

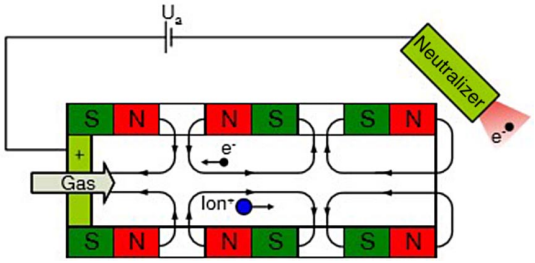

Fig. 1 Principle of HEMP-T [6].

ring-shaped permanent periodic magnets (PPMs) aligned coaxially along the chamber with reversing polarity to produce the cusps between the magnets is used to confine the plasma beam. Electrons are magnetized and follow the magnetic field lines gyrating around them with their Larmor radius [7,8]. Due to the structure of the magnetic configuration, they oscillate between the cusps that form a magnetic mirror. This enhances strongly the ionization efficiency of the neutral gas [8]. Ions have a much larger mass, and are therefore not magnetized [8,9]. However, they follow the electrons and are electrostatically confined because a plasma has to approach quasi neutrality [10]. Only at the cusp, the plasma has wall contact due to radial magnetic field lines; whereas within the cusps, the magnetic field lines are axially formed [7,8]. Close to the axis, the axial field lines lead to dominant parallel electron transport that produces an axial potential profile; and then it drops at the exit of the thruster where the electron confinement is lost [10]. Ions experience this electric field and are accelerated out of the thruster, generating the thrust. Wall contact is minimized to the cusp regions; due to the radial structure of the electric field with rather small potential drops, the energies of impinging ions are below the sputter threshold and erosion is omitted [10].

There has been some effort made to scale down EP for specific microsatellites and deep-space exploration because a miniature concept of the CFT would offer better performance over current full-scaled EP thrusters in terms of weight reduction and propellant consumption. This would subsequently result in savings on the launch cost for satellites. However, the previous experimental data of downscaled EP revealed significantly low performance due to the complexity of the EP system [6]. The main problem arises in the complex interaction of the plasma beam with the magnetic field, anode current, anode power, mass flow rate, and geometric considerations.

Herein, a multiobjective design optimization (MDO) study, based on evolutionary algorithms, has been conducted, aiming to simultaneously maximize three objectives, i.e., thrust, total efficiency, and specific impulse of the CFT configuration so as to fulfill such design requirements for a downscaled EP. The optimization has been performed by employing the surrogate models that have been trained, based on the results from an initial MDO run using a chain process that incorporates magnetic field analysis coupled with power distribution calculation into evolutionary algorithms. Selected CFT designs have been examined to gain insights into key design factors and underlying mechanism and physics. Further investigation has been conducted to verify the performance by means of a particle-in-cell simulation that accounts for kinetic effects for accurate analysis of the physics and performance.

II. Methodology

A. Multiobjective Design Optimization

MDO is performed in a chain process consisting of sequential phases, as shown in Fig. 2 [11]. Each process is described in detail, following general descriptions of that MDO. This approach enables robust and efficient population-based optimization by employing evolutionary algorithms, particularly the nondominated sorting genetic algorithm (known as NSGA-II), at reasonable computational cost by approximating the performance with surrogate modeling in lieu of expensive computational evaluation [12].

The population size needs to be chosen to effectively explore the design space represented by the decision variables to identify optimum solutions with respect to the objectives functions within reasonable computational effort. Recombination operations (i.e., simulated binary crossover and polynomial mutation) are used at a given probability (1.0 and 0.1, respectively, in this study) with a specified distribution index (10 and 20, respectively) to the decision variables at the previous generation [13]. The use of a nondominated sorting genetic algorithm always retains the best solutions across generations offering to use the simulated binary crossover and polynomial mutation to broaden the search for better solutions; hence, the crossover probability is given by 1.0 [12].

Surrogate modeling is employed to estimate values of the objectives and constraints in an efficient manner. This mimics the behavior of the solutions with metamodels characterized by appropriate mathematical functions based on the simulation models [14]. In this study, a surrogate fraction (which is 90% of the evaluated solutions calculated from the actual simulation models) is applied to prevent overfitting, whereas the remainder of the evaluated solutions is used to assess the performance of the actual surrogate models [13]. A subset of the archive for surrogate training is created by selecting the solutions closest to the centroids of the k clusters obtained through k-means clustering [15]. The data are used to train the surrogate models for each of the objective and constraint functions [15]. Multiple surrogate models are employed to evaluate the best possible solutions: a quadratic response surface model; artificial neural network (ANN) models including the radial basis function network and multilayer perceptron models, which are single-layer and feedforward types of ANN models, respectively; and a kriging model based on Gaussian process regression [16–19]. The mean squared error (MSE), which is calculated for the remaining solutions (10%) based on the actual and predicted values of the objectives and constraints, is used as the tool to validate the surrogate models. The best surrogate prediction is adopted to replace the actual simulation analysis on the conditions that the MSE is within a threshold value of 5% for all objective and constraint functions and that the distance to the closest point in the archive is smaller than 5% [13].

A variance-based global sensitivity analysis is performed to examine the influence of each decision or input variable x_i on the objective function or output parameters y [14]. The quasi-random numbers build a sample quantity of 10,000 as the input matrices $\boldsymbol{X}$ for each variable and produce multiple columns for the decision variables with the given ranges [20]. The input matrices are assessed within the surrogate model to predict the output vectors $\boldsymbol{Y}$ accurately. The first-order indices S_i and total-effect indices S_{T_i} in Eqs. (1) and (2) are calculated by the method described in Ref. [21]:

$$S_i = V[E(Y|X_i)]/V(Y) \tag{1}$$

$$S_{T_i} = 1 - V[E(Y|X_{-i})]/V(Y) \tag{2}$$

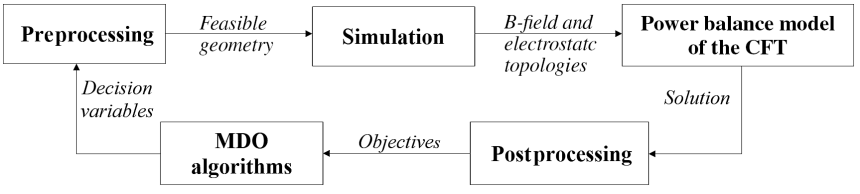

Fig. 2 MDO process chain [11].

The variable-magnet-length cusped field thruster from the available literature is used to validate this approach because it considers the physical dimensions and material properties for the thruster, and the subsequent analysis of the results provides a robust range of observation points that can be modeled and compared [4] (readers are referred to Ref. [11] for validation).

1. *Preprocessing*

The decision variables or input variables are examined in the preprocessing phase to assure the model is geometrically feasible before the simulation.

2. *Simulation*

ANSYS Maxwell [22] constructed a model for the given geometry and calculated the magnetic field strength topology at the dielectric wall and the center of the chamber by means of magnetostatic analysis, and then the electrostatic analysis was performed to calculate the potential at the thruster exit and in the plume.

CFT operation is mainly characterized by the PPMs that are used to create the magnetic mirror effect to reduce electron losses due to impingement on the walls, as prescribed by the Lorentz force equation in Eq. (3). It follows that the magnetic field does not have impact on the particle directly, but it exerts longitudinal axial force F_z when its strength increases in the opposite direction of its motion with constant kinetic energy K [1,23–25]:

$$F_z = \frac{m\nu_\perp^2}{2B}\nabla_\parallel B \tag{3}$$

The magnetic moment is constant by equating and balancing the magnetic moment at the high- and low-field regions when the particle is moving through a magnetic field of increasing strength:

$$\frac{\nu_{\perp 0}^2}{B_0} = \frac{\nu_{\perp m}^2}{B_m} \tag{4}$$

where subscripts 0 and m refer to low- and high-field regions, respectively.

The equation of velocity of the particle can be solved by conservation of the particle kinetic energy:

$$K = \frac{1}{2}m(\nu_\parallel^2 + \nu_\perp^2) \tag{5}$$

Therefore,

$$\nu_\parallel = \left[\frac{2}{m}(K - \mu B)\right]^{1/2} \tag{6}$$

To ensure the magnet mirror effect, the vector of the velocity is required to be within an acceptable angle, and the equation can be solved using the conservation of kinetic energy, which is derived as follows [24]:

$$\frac{B_m}{B_0} = \frac{\nu_{\parallel 0}^2 + \nu_{\perp 0}^2}{\nu_{\perp 0}^2} = \frac{1}{\sin^2\theta_m} \tag{7}$$

Therefore,

$$\theta_m \le \sin^{-1}\left(\frac{\sqrt{B_0}}{\sqrt{B_m}}\right) \tag{8}$$

The arrival probabilities of the electrons at each cusp region can be determined as follows [7]:

$$P_c = \frac{2\pi\int_0^{\theta_{mc}}\sin\theta\,\mathrm{d}\theta}{4\pi} \tag{9}$$

where subscript c refers to the position of the cusps.

The cusp arrival probabilities are sensitive to the accuracy of the simulated magnetic topologies of the thruster, which are calculated using the two-dimensional electromagnetic field analysis. Based on the magnetic mirror effect described in Eqs. (7) and (8), the ratio of the magnetic topologies between low and high regions is used to compute the cusp arrival probability for each location throughout the thruster.

3. *Power Balance Model*

The calculated probabilities and input variables are subsequently passed on to be used in the power balance calculation. A simplified power balance model of the HEMP-T, shown in Fig. 3, describes a one-dimensional system with 28 equations based on the plasma fluid theory. These equations, given by Kornfeld et al. [7], can be solved simultaneously to allow for a reasonable estimate of the essential properties for the thruster performance.

The set of equations can be solved through only a few input parameters, such as an anode voltage U_a; an anode current I_a; and the ratio of the magnetic field strength from the axially aligned regions to where the field radially crosses the discharge wall, i.e., the magnetic mirror strength [11]. The magnetic field strength is used to calculate the cusp arrival probabilities, which indicate probabilities of electrons reach dielectric wall at cusp locations. It is also important to note that the ratios of the energy transferred to excitation, ionization, and thermalization are only estimations, as per Ref. [7], where a full description of the power model can be found. The general performance equations are used to calculate the thruster performance by applying the parameters gained from the power balance model:

$$\eta_t = \frac{T^2}{2\dot{m}P_{\text{in}}} \tag{10}$$

$$\eta_a = \frac{T^2}{2\dot{m}_a P_a} \tag{11}$$

The total efficiency is generally defined by the ratio of the produced thrust to the input power in Eq. (10); but, for the HET, the anode efficiency is generally defined as in Eq. (11) [26]:

$$\eta_v = \frac{U_b}{U_a} \tag{12}$$

$$\eta_b = \frac{P_b}{P_a} = \frac{I_b}{I_a} \tag{13}$$

$$\eta_m = \frac{I_b}{\dot{m}_a q/m} \tag{14}$$

$$\eta_a = \frac{1}{Q^2}\eta_v\eta_b\eta_m\cos^2\theta_{\text{eff}} \tag{15}$$

The anode efficiency η_a in Eq. (11) can also be divided into the efficiency components, such as voltage efficiency η_v, beam efficiency η_b, utilization efficiency η_m, and the coefficient of plume divergence. They are more measurable and are used to calculate the anode efficiency accurately, as per Eq. (15). The beam efficiency η_b is the ratio of power at the anode to the power at the plasma beam;

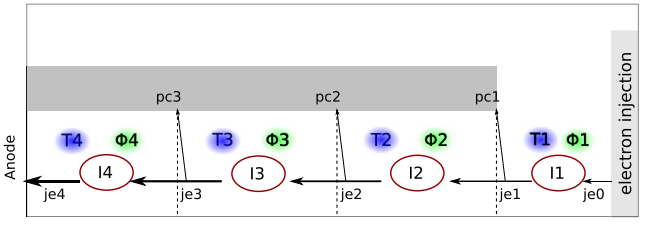

Fig. 3 Schematic of CFT with the most important quantities for the power balance model [7].

and the utilization efficiency η_m is the maximum current obtainable from the supplied beam current, assuming only singly charged ions. Due to the divergence of the ion beam with the effective divergent angle θ_{eff}, the coefficient of the plume divergence is required to solve the proper relation of propulsion [1].

From Goebel and Katz [1], the beam current is sensitive and proportional to the ionized mass flow rate:

$$I_b = \frac{q\dot{m}_i}{m} \tag{16}$$

The propellant is assumed to be xenon, which is typical for a CFT with a high-voltage operational range, which is typically between 500 and 2000 V [5]. Lower efficiencies under the same mass flow rate conditions were found with the anode voltage below 500 V [4,5]; thus, this study was not able to take the effects of low ionization into account. Equation (15) is a basic equation that assumes singly charged ions for the HET, whereas it would not fully describe low ionization at low voltages and multiply charged ions at high voltages, which could occur in practical applications.

The mass utilization efficiency, described in Eq. (14), is sensitive to the beam current and mass flow rate. As a result, this study assumes that the ion beam current can be sufficiently approximated by Eq. (13). The mass utilization efficiency correction factor to consider the effect of multiply charged ions is given by α_m in Eq. (17) [1]:

$$\alpha_m = \frac{1 + (1/2)(I^{++}/I^{+})}{1 + (I^{++}/I^{+})} \tag{17}$$

$$\eta_m = \alpha_m \frac{I_b}{q}\frac{m}{\dot{m}_a} \tag{18}$$

The rest of the performance parameters are calculated based on anode efficiency by using the general thruster performance equations listed in the following:

$$I_{\text{sp}} = \frac{T}{\dot{m}_a g} \tag{19}$$

$$P_a = \frac{1}{2}\dot{m}_a v^2 = U_a I_a \tag{20}$$

$$\text{PTTR} = \frac{P}{T} = \frac{U_a I_a}{I_a\sqrt{2(m/q)U_a}} = \sqrt{\frac{qU_a}{2M}} \tag{21}$$

where PTTR denotes the power-to-thrust ratio in watts per newton.

4. *Postprocessing*

The resultant solutions from the power balance calculation are postprocessed to deliver the objectives and assess if they lie within the set of physical constraints. As the MDO does not consider the effects of multiple ion species on the correction factor, the acceleration, and the plume divergence efficiency, they are difficult to determine accurately with the present methodology. The additional assumptions from the available literature are used to take into account of the effect of 20% doubly charged ions in the mass utilization efficiency ($\alpha_m = 0.9$) [5] and other assumptions made regarding the acceleration, divergence, and utilization efficiencies in the postprocessing phase. The plume divergence efficiency is based on an assumed divergence angle of 60 deg [5]. The acceleration efficiency requires significant measurement of the CFT, which is beyond the scope of this study. Keller et al. presented a combined acceleration and divergence efficiency of 40.7% (i.e., $\eta = \eta_{\text{acc}} \cdot \eta_{\text{div}} = 0.407$) by extrapolating the acceleration efficiency from the Faraday measurement values [5].

5. *MDO Algorithms*

The calculated values of the objective functions and the feasibility assessment are then submitted to the MDO algorithms for evaluation toward the next generation. This iterative cycle continues, yielding more designs to be evaluated according to the set criteria.

B. Thruster Modeling

The initial MDO with a population size of $N = 64$ is performed by employing evolutionary algorithms over 50 generations, and then the surrogate prediction is performed with $N = 100$ to be evolved over 100 generations. This allows us to explore the design space for an optimization problem with three objectives and five decision variables with reasonable computational effort.

Three objective functions are considered and employed to evaluate the design performance, namely, the thrust T, specific impulse I_{sp}, and total efficiency η_t. The efficiency measures described in Eq. (15) are used to calculate the anode efficiency η_a, which is regarded as the total efficiency η_t within the present thruster model. (The efficiency term with the subscript t might be somewhat of a misnomer because it is usually descriptive of the total efficiency. Also, it must be noted that the model presented in this paper does not take into consideration the plume divergence losses or give an accurate representation of the acceleration efficiencies [11].) A simplified two-dimensional CFT model is used for the calculations using ANSYS Maxwell to mitigate the computational load, which would otherwise be expensive due to the nature of the MDO process, and to facilitate the identification of the relationships between the output objectives and the decision variables. The magnetic radii [inner magnetic radius (IMR) and outer magnetic radius (OMR)] are used to calculate the strength of the magnetic field in the high and low regions, which are solved through the one-dimensional simplified power balance model describing the plasma potentials, cusp potentials, ionization source currents, and electron and ion currents across plasma cells that divide the discharge chamber length, as described in Sec. II.A.3. The other decision variables of U_a (in volts), I_a (in amperes), and $\dot{m}_a$ (standard cm^3/min) are used to solve the objective functions through Eqs. (15–21) and represent the initial conditions of the CFT at the anode. As a consequence, the beam and grid efficiencies are determined; and power losses due to ionization and excitation are calculated at the anode and the cusps, which impact the objective functions. The optimization statement is thus summarized in Table 1, along with the ranges of the decision variables.

The model assuming axisymmetry at the engine axis consists of a consistently straight chamber made of boron nitride ceramic, samarium–cobalt 27 MG·Oe magnets with spacers made of pure iron (due to high conductivity and to improve commonality with other CFT design), and the thruster housing made of 6061-T6 aluminum [5,27–29]. Geometric constraints are applied to restrict the scope and output of the design space, including geometries (inner magnetic radius and outer magnetic radius). Designs with geometries that overlap are deemed infeasible solutions in MDO. The upper limits of the design variables are set based on the experimental studies [4,5,7] and are assumed within the limits of the standard CubeSat design (i.e., a 100 mm cube (1U)) [30].

C. Particle-In-Cell Simulation

In the CFTs considered in this work, the electron distribution function in the discharge channel is determined by magnetized electrons and kinetic effects such as reflection at the magnetic cusps. Moreover, the mean free path of the dominant electron collision type (i.e., elastic collisions with neutral xenon atoms) is on the scale of the channel length, which is too large to thermalize the electron

Table 1 Optimization problem

Maximize	Subject to
T, η_t, I_{sp}	$0 \le U_a(\text{V}) \le 1000$
	$0 \le I_a(\text{A}) \le 10$
	$0.2 \le \dot{m}_a(\text{standard cm}^3/\text{min}) \le 50$
	$2 \le \text{IMR(mm)} \le 15$
	$2 \le \text{OMR(mm)} \le 28$

energy distribution. As a result, the electron energy distribution is non-Maxwellian throughout the discharge channel; and a fully kinetic particle model is required for accurate analysis [31]. Due to the axisymmetric problem, a two-dimensional particle-in-cell (PIC) code with cylindrical $(r-z)$ coordinates and three dimensions in the velocity space is used in conjunction with a Monte Carlo collision (MCC) model [32].

The number of particles in the real plasma is so large that it exceeds the capacity that can be handled even by supercomputers. Therefore, the present PIC simulations consider a single particle (so-called superparticle) consisting of many plasma particles. Because the charge/mass ratio of the superparticle is the same as the actual particle, the particle trajectories are also the same as those of individual plasma particles. Consequently, the plasma model simulated using superparticles is the same as that of the real plasma with appropriate rescaling of parameters. The dynamics of neutral propellant atoms [xenon (Xe)], electrons (e^-), as well as Xe^+ and Xe^{2+} ions are treated as superparticles. In the measurements of other CFTs, the density of multiply (triply or higher) charged xenon ions is considerably lower than that of doubly charged ions [33]. Based on these observations, multiply charged xenon ions are neglected for this work too.

To simulate the real plasma, the force on the particles has to be calculated self-consistently. The potential and the electric field are calculated on a spatial grid based on the charge of the superparticles mapped on the grid points by means of charge weighting. The calculated fields and forces are mapped from the grid points to the particle positions, called field weighting, using the same weighting function as before to preserve the energy and impulse. The superparticles are moved according to the Lorentz force using the Boris algorithm [34]. The new particle positions and velocities are calculated by considering the thruster boundary conditions.

Although the mean free paths of the particle collisions are at least on the scale of the discharge channel length, correct representation of the collision processes is necessary for accurate modeling of the particle distribution functions. The spatial distribution of ionization processes, which are determined by the high-energy tail of the electron energy distribution function, strongly influences the global properties of a CFT, such as the discharge current and thrust. The PIC model therefore includes an MCC module for accurate representation of the dominant collision processes in the thruster. In the present study, electron–electron Coulomb collisions are simulated directly [35], and all other collisions are modeled with experimentally measured collision cross sections [36]. These collisions are the direct single and double e^-–Xe impact ionizations, the single e^-—Xe^+ impact ionization, the integral elastic Xe^+–Xe collisions (including charge exchange and momentum transfer), and the integral elastic and inelastic e^-–Xe collisions [32]. An electrostatic model is used because the magnetic field contribution from the plasma currents can be neglected.

In the simulation model, the entire thruster discharge channel and a part of the near-field plume are considered. For computational feasibility, similarity scaling is used to simulate the system. It is designed to leave the physical behavior within the thruster channel (where electrons are magnetized) unchanged, and thus the Hall parameter and the Knudsen number of the system are preserved. The similarity scaling scales down the system size and time linearly, whereas the velocities and densities remain unscaled. A closer description of the similarity scaling scheme can be found in Ref. [32], and a full description of the PIC setups including the boundary conditions employed in the present study can be found in Ref. [8].

The geometric quantities used in the present simulation are an inner magnetic radius of 9.91 mm, an outer magnetic radius of 25.10 mm, and a channel length of 21 mm. Based on an electron density of 1×10^{14} cm^{-3} and a mean electron temperature of 10 eV inside the channel, the Debye length and the plasma frequency are calculated; and they are used to calculate the grid spatial resolution of 1.76×10^{-4} cm and a time step of 8.9×10^{-14} s. The domain size of 20×50 mm is selected to resolve the channel and near-exit region, resulting in a cell resolution of 283×709 cells. For the simulation, the anode voltage is set at 1000 V and is located at the anode at the left domain boundary. The right domain boundary at 50 mm is set as a constant electric field. The neutral xenon propellant source is located at the center of the anode, and it is injected into the thruster channel at a mass flow rate of 50 standard cm^3.

III. Results

Figure 4 presents the results obtained from the MDO after evolution over 100 generations performed by using the surrogate models that have been built based on the initial MDO performed by employing ANSYS Maxwell for magnetostatic analysis. The green points indicate the feasible geometries, and the blue points represent nondominated solutions (also known as Pareto-optimal solutions) where none of the objective functions can be improved without sacrificing one or more of the other objective functions. The set of Pareto-optimal solutions is called a Pareto-optimal front, which is indicative of the counteracting nature of the objective functions. Presented in Fig. 5 is the parallel coordinate plot that visualizes the trends and relations among the decision variables and the objective and constraint functions for the nondominated solutions identified by the MDO, which are indicated by light blue lines. The design point S_1 selected from the nondominated solutions (presented in Table 2) is denoted by a red line. Other blue lines represent all designs that have been considered and evaluated in each generation in the evolutionary MDO process.

S_1 has been postprocessed to take into account the acceleration efficiency, the divergence efficiency, and the doubly charged ions by applying the aforementioned assumptions in Sec. II.A.4, as shown in Table 3. This produces a more conservative estimation of the objective parameters. The representative solution S_1 is characterized by decision variables of the mass flow and anode potential at their upper limits and features the most balanced performance among all designs. Its values of the decision variables are used for PIC analysis to verify the output parameters by accurately accounting for phenomena and performance losses that MDO was not able to consider.

Tables 4 and 5 display the first-order indices S_i and the total-effect indices S_{T_i} identified by the covariance-based sensitivity analysis performed for both magnetic configurations. They quantitatively indicate the main and overall effects of the input parameters (i.e., decision variables), namely, U_a, I_a, $\dot{m}_a$, IMR, and OMR on the output parameters (i.e., objective functions), namely, thrust T, total efficiency η_t, and specific impulse I_{sp}. The difference between the total-effect index S_{T_i} and the first-order index S_i is indicative of the degree of the influence of the decision variable in combination with other decision variables (i.e., interactions) on the objective functions [20]. If the decision variables are characterized by the sum of both

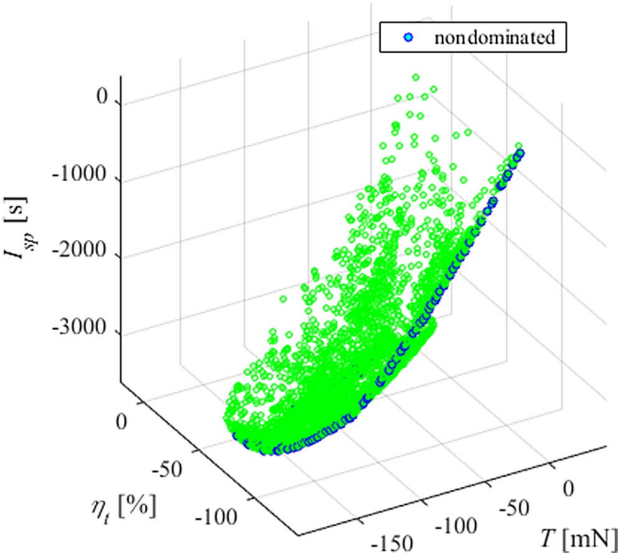

Fig. 4 Optimization results from MDO [11]. Test data for thrust, efficiency, and specific impulse are along x, y, and z axes. Negative sign denotes a maximization problem.

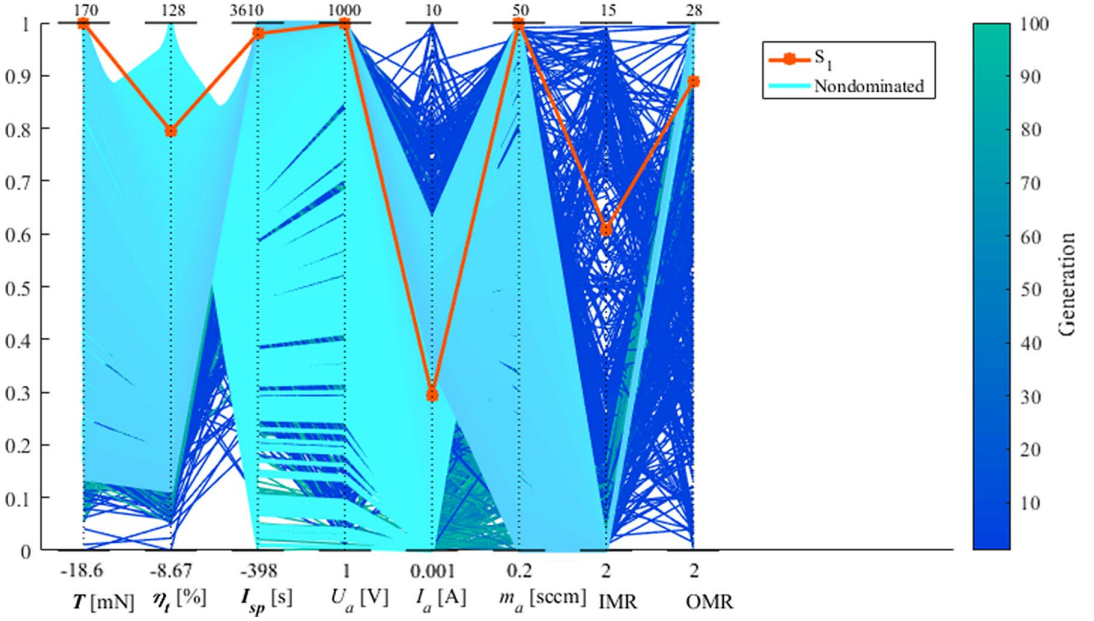

Fig. 5 Parallel coordinate plot. Selected design point is denoted by a red line among nondominated solutions represented by light blue lines, whereas other lines indicate designs evaluated in the course of MDO.

first-order and total-effect indices being near unity (i.e., $\sum S_i \approx 1$ and $\sum S_{T_i} \approx 1$), it follows that the effects of individual decision variables are linearly additive. The sensitivity indices indicate that the influence on the design is primarily caused by four design parameters, i.e., I_a, OMR, IMR, and $\dot{m}_a$. I_a exerts the most influence on specific impulse I_{sp}, whereas the OMR predominantly influences the total efficiency. It is evident that the decision variables exhibit similar influence across the three objectives, as expected by Eq. (11). The considerably large difference between the summations of S_i and S_{Ti} is indicative of the highly nonlinear behavior between the design variables and the output parameters.

The large influence of the mass flow rate $\dot{m}_a$ and the anode current I_a is inherently expected due to the highly interrelated nature of the calculation of total efficiency η_t that involves and relies on these parameters. The beam efficiency η_b represents a primary source of the efficiency loss, and is thus directly sensitive to anode current, as per Eq. (13) [25]. Furthermore, the beam current is strongly related to the mass flow rate due to Eq. (16) [1,37,38]; and assessment of the influence of these decision variables (design parameters) on the objective functions (performance parameters) offers flexibility in identifying the designs to achieve optimal performance. The sizable influence of the outer and inner magnet radii is assumed to be attributed to their influence on the magnetic field strength due to geometric variation, whereas further investigation would be necessary to verify this. It is important to note that other measures for the efficiency (such as the mass utilization, acceleration efficiency, and divergence losses) are not taken into consideration in the present model (as mentioned in Sec. II.A.3) and would need to be estimated or deduced from existing experimental studies.

An additional MDO study using the modified models has been conducted to assess the updated performance on the selected design configuration presented in Table 6 upon careful investigation and comparison of the original MDO and PIC simulation results. This has revealed physical characteristics of the beam that allow us to improve the accuracy of the solution within a reasonable difference from the PIC result. Further details are presented in Sec. IV.

Table 2 Configuration of the selected design S_1 (denoted by the red line in Fig. 5) [11]

Solution (original)	S_1
T, mN	169.9
η_t, %	99.6
I_{sp}, s	3526
U_a, V	999.9
I_a, A	2.94
$\dot{m}_a$, standard cm^3/min	49.98
IMR, mm	9.91
OMR, mm	25.10

Table 3 Adjusted performance of the selected design S_1 by taking account of $\eta = \eta_{\text{acc}} \cdot \eta_{\text{div}} = 0.407$ in postprocess [11]

Solution (original)	S_1
T, mN	102.7
η_t, %	36.5
I_{sp}, s	2131

IV. Discussion

The PIC simulation of the S_1 configuration has shown a typical behavior of CFT thrusters, as discussed in the preceding section. With the full kinetic description from the PIC results, it is now possible to calculate the performance parameters considered in the MDO in a self-consistent manner. Table 7 compares the values for performance

Table 4 First-order sensitivity indices [11]

Parameter	U_a	I_a	$\dot{m}_a$	IMR	OMR	Sum
T	0.015	0.084	0.050	0.018	0.072	0.239
η_t	0.007	0.051	0.026	0.042	0.153	0.279
I_{sp}	0.009	0.097	0.034	0.036	0.167	0.343

Table 5 Total-effect sensitivity indices [11]

Parameter	U_a	I_a	$\dot{m}_a$	IMR	OMR	Sum
T	0.111	0.597	0.430	0.433	0.565	2.136
η_t	0.165	0.549	0.328	0.363	0.702	2.107
I_{sp}	0.089	0.644	0.308	0.409	0.600	2.050

Table 6 Updated performance of the S_1 design after PIC

Solution (modified)	S_1
T, mN	62.8
η_t, %	15.2
I_{sp}, s	1333

Table 7 Comparison of operation parameters of the S_1 design between original MDO and PIC results

	I_a, A	I_b, A	T, mN	η_t, %	I_{sp}, s
MDO (original) [11]	2.94	3.61	102.7	36.5	2131
PIC [8]	2.66	2.30	62.8	15.2	1333
Difference, %	9.5	36.3	38.9	58.3	37.4

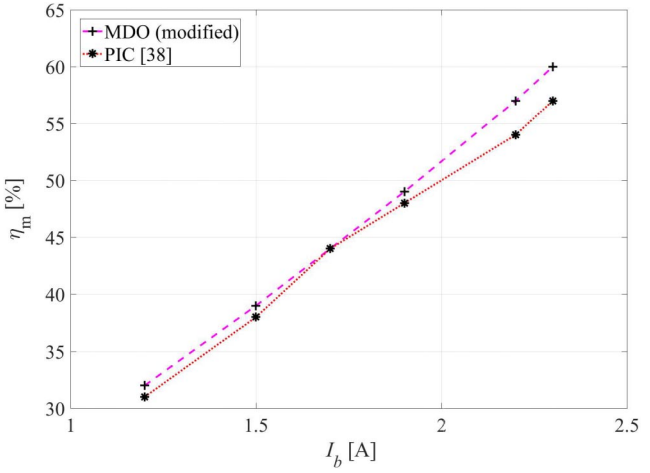

Fig. 6 Influence of beam current I_b on mass utilization efficiency η_m for the modified MDO model and PIC simulation.

parameters as well as the anode and beam currents between the modeling used in MDO and the calculations from the PIC simulation.

The higher beam current of MDO displayed in Table 7, in comparison to that of the PIC, is attributed to the theoretical prediction based on Eq. (16). The over prediction of beam current has subsequently led to higher performance values in MDO than those from PIC with respect to thrust, total efficiency, and specific impulse. The performance discrepancies between MDO and PIC are comparable for the beam current, thrust, and specific impulse.

This observation has led to further investigation on the influence of the key parameters so as to improve the accuracy of the models

Table 8 Comparison of averaged plume divergence angle of the S_1 design between modified MDO prediction and PIC simulation

I_a, A	Divergence angle (modified MDO), deg	Divergence angle (PIC) [8], deg	γ ($\cos^2\theta_{\text{eff}}$ ratio)
1.27	44.5	43.2	1.04
1.59	46.9	46.8	1.00
1.81	48.6	49.1	0.98
2.04	50.4	50.9	0.98
2.45	53.6	52.7	1.04
2.66	55.2	53.6	1.08

and to examine the validity of applying the specific data obtained from the PIC simulation. It is noteworthy to reiterate here that the beam current obtained from MDO is much higher than that from the PIC simulation, and the mass utilization efficiency plays a key role in the determination of the thruster performance as per Eq. (15).

The efficiency ratio η_a/η_m can be derived based on Eq. (15) and can be expressed as a function of three parameters, i.e., the beam current, beam potential, and divergence angle, which are subject to some uncertainties. This ratio allows for the identification of the source of the difference observed between the MDO and PIC results by examining their influence in isolation.

Figure 6 compares the behavior of the beam current in response to the mass utilization efficiency in the modified MDO model based theoretically on Eq. (16) and that based on the full kinetic analysis using a PIC simulation. Considerable agreement can be seen between the two results, with the maximum difference being 4% at the highest beam current.

Figure 7 displays the variations of the thruster performance with respect to the mass utilization efficiency obtained from a parametric study of MDO (modified) and the PIC. Figure 7a shows consistently similar trends for the thrust values, whereas Fig. 7b presents a somewhat different behavior for the anode efficiency.

The influence of the plume divergence angle is presented in Table 8 in terms of the ratio of the squared cosine of the divergence angle, i.e.,

$$\gamma \equiv \frac{\cos^2\theta_{\text{eff}}\ (\text{PIC})}{\cos^2\theta_{\text{eff}}\ (\text{MDO})}$$

The divergence angles for the PIC simulation are evaluated for every particle in the given current conditions. The emission angles become large with the current [8]. The peak emission angles of the modified MDO runs can be approximated as $\theta_{\text{eff}} = 7.7I_a + 34.7$ by linear regression of the results from the PIC simulation [8]. This yields more accurate prediction of the divergence angles as compared to the case with the assumption of the divergence angle described in Sec. II.A.4. It can be seen that a maximum error of 8% due to the divergence angle occurs at the highest anode current.

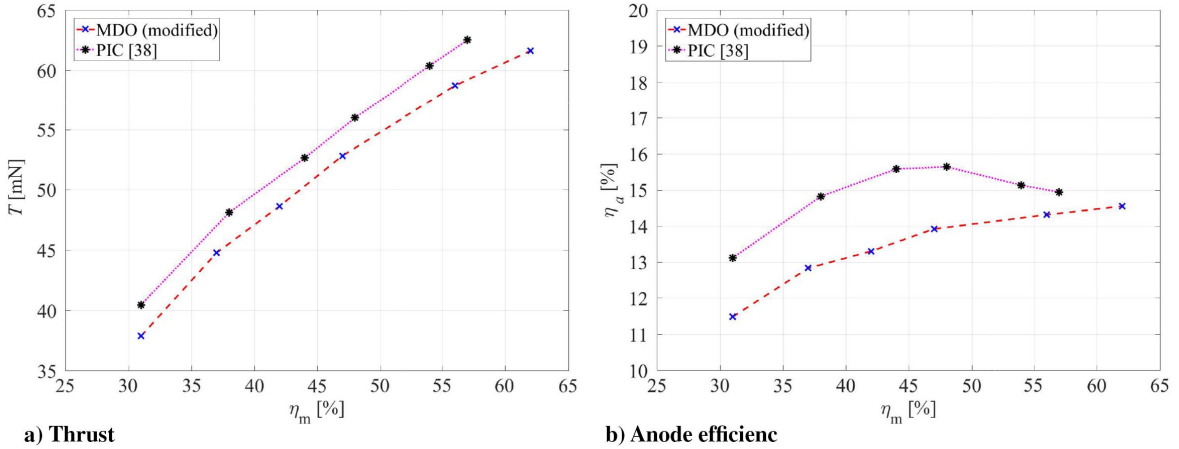

a) Thrust **b) Anode efficienc**

Fig. 7 Influence of mass utilization efficiency η_m on thruster performance for the modified MDO model and PIC simulation.

Table 9 Comparison of operation parameters of the S_1 design between modified MDO prediction and PIC simulation

	I_a, A	I_b, A	T, mN	η_t, %	I_{sp}, s
PIC [8]	2.66	2.30	62.8	15.2	1333
MDO (modified)	2.66	2.36	61.7	14.6	1280
Difference, %	— —	2.5	1.8	4.1	4.1

Table 9 compares the operation parameters and performance difference by applying the values calculated from the PIC to the modeling used for MDO (modified), indicating that the maximum difference between the MDO prediction and the PIC simulation has reduced to 4.1%. This considerable improvement is attributed to the improved estimations of the beam current presented in Fig. 6 and the divergence angle in Table 8, which allowed us to enhance the fidelity of the thruster performance in the modified MDO model. The remainder of the performance difference was assumed to originate from the uncertainties associated with the beam potential, where analytical estimation of the beam potential represented difficulty because it was primarily based on theoretical assumptions in the modeling for MDO. The full kinetic analysis by PIC simulation has enabled accurate calculation of the beam potential due to every particle.

V. Conclusions

The representative point has been selected from the resultant Pareto-optimal front, which is identified as a candidate for optimal CFT design to achieve the most desirable performance metrics. A kinetic analysis has been performed by means of a PIC simulation for the selected design in order to verify the results from the MDO study by accurately accounting for the performance losses associated with the uncertainties and complexities of the CFT design and phenomena.

Qualitative coherence has been observed between the PIC solution and the MDO result for the performance metrics and other key parameters, whereas considerable differences have been found quantitatively, suggesting room for improvement is left in the modeling of CFT performance to enhance prediction accuracy.

Further detailed investigation has been undertaken by probing into the results from the PIC simulation so as to improve the performance modeling for MDO. The influence of the modeling uncertainties has been examined quantitatively for the beam current, beam potential, and divergence angle, which have been identified to be responsible for the performance differences. The application of the values from the full kinetic description using the PIC simulation for these parameters has significantly reduced the prediction errors of the thruster performance to less than 5% in the MDO modeling. This underlines the importance of reliable estimation and modeling of these properties in order to enable physics-based MDO studies for CFT downscaling by reasonably taking key physical characteristics into account.

Acknowledgments

Suk Hyun Yeo is grateful for the support by the Australian Government Research Training Program Scholarship. The work of Paul Matthias, Daniel Kahnfeld, and Ralf Schneider has been sponsored by the DLR, German Aerospace Center through project 50RS1510. The authors are also thankful to Angus Muffatti and Thomas Fahey for the original development of the optimization process chain incorporating the performance analysis and magnetic field simulations. They are grateful to Tapabrata Ray at the University of New South Wales for the original multiobjective design optimization framework developed in the group.

References

[1] Goebel, D. M., and Katz, I., *Fundamentals of Electric Propulsion: Ion and Hall Thrusters*, Vol. 1, Wiley, Hoboken, NJ, 2008, pp. 1–14, 15–34, 37–90, Chaps. 1, 2, 3. https://doi.org/10.1002/9780470436448

[2] Van Noord, J., "Lifetime Assessment of the NEXT Ion Thruster," *43rd AIAA/ASME/SAE/ASEE Joint Propulsion Conference and Exhibit*, AIAA Paper 2007-5274, July 2007. https://doi.org/10.2514/6.2007-5274

[3] Boyd, I. D., "Simulation of Electric Propulsion Thrusters," Univ. of Michigan TR RTO-EN-AVT-194, Ann Arbor, MI, 2011.

[4] Ma, C., Liu, H., Hu, Y., Yu, D., Chen, P., Sun, G., and Zhao, Y., "Experimental Study on a Variable Magnet Length Cusped Field Thruster," *Vacuum*, Vol. 115, May 2015, pp. 101–107. https://doi.org/10.1016/j.vacuum.2015.02.007

[5] Keller, A., Köhler, P., Hey, F. G., Berger, M., Braxmaier, C., Feili, D., Weise, D., and Johann, U., "Parametric Study of HEMP-Thruster Downscaling to μN Thrust Levels," *IEEE Transactions on Plasma Science*, Vol. 43, No. 1, 2015, pp. 45–53. https://doi.org/10.1109/TPS.2014.2321095

[6] Keller, A., Kohler, P., Feili, D., Berger, M., Braxmaier, C., Weise, D., and Johann, U., "Feasibility of a Down-Scaled HEMP Thruster," *32nd International Electric Propulsion Conference*, IEPC-2011-138, Verlag Dr. Hut, Wiesbaden, Germany, Sept. 2011.

[7] Kornfeld, G., Koch, N., and Harmann, H.-P., "Physics and Evolution of HEMP-Thrusters," *Proceedings of the 30th International Electric Propulsion Conference*, IEPC-2007-108, Florence, Italy, Sept. 2007, pp. 17–20.

[8] Matthias, P., Kahnfeld, D., Schneider, R., Yeo, S. H., and Ogawa, H., "Particle-in-Cell Simulation of an Optimized High-Efficiency Multistage Plasma Thruster," *Contributions to Plasma Physics*, Vol. 59, No. 9, 2019, Paper e201900028. https://doi.org/10.1002/ctpp.201900028

[9] Eichmeier, J. A., and Thumm, M., *Vacuum Electronics: Components and Devices*, Springer Science and Business Media, New York, 2008, pp. 288–301, Chap. 6.4.

[10] Brandt, T., Scheider, R., Duras, J., Kahnfeld, D., Hey, F. G., Kersten, H., Jansen, F., and Braxmaier, C., "Particle-In-Cell Simulation of a Down-Scaled HEMP Thruster," *Transactions of the Japan Society for Aeronautical and Space Sciences, Aerospace Technology Japan*, Vol. 14, No. ists30, 2016, pp. Pb_235–Pb_242. https://doi.org/10.2322/tastj.14.Pb_235

[11] Fahey, T., Muffatti, A., and Ogawa, H., "High Fidelity Multi-Objective Design Optimization of a Downscaled Cusped Field Thruster," *Aerospace*, Vol. 4, No. 4, 2017, Paper 55. https://doi.org/10.3390/aerospace4040055

[12] Deb, K., Pratap, A., Agarwal, S., and Meyarivan, T., "A Fast and Elitist Multiobjective Genetic Algorithm: NSGA-II," *IEEE Transactions on Evolutionary Computation*, Vol. 6, No. 2, 2002, pp. 182–197. https://doi.org/10.1109/4235.996017

[13] Ray, T., Isaacs, A., and Smith, W., "Multi-Objective Optimization Using Surrogate Assisted Evolutionary Algorithm," *Introduction, Multi-Objective Optimization: Techniques and Applications in Chemical Engineering*, edited by G. P. Rangaiah, World Scientific, Singapore, 2008, pp. 131–151. https://doi.org/10.1142/9789812836526_0005

[14] Queipo, N. V., Haftka, R. T., Shyy, W., Goel, T., Vaidyanathan, R., and Tucker, P. K., "Surrogate-Based Analysis and Optimization," *Progress in Aerospace Sciences*, Vol. 41, No. 1, 2005, pp. 1–28. https://doi.org/10.1016/j.paerosci.2005.02.001

[15] Lloyd, S., "Least Squares Quantization in PCM," *IEEE Transactions on Information Theory*, Vol. 28, No. 2, 1982, pp. 129–137. https://doi.org/10.1109/TIT.1982.1056489

[16] Box, G. E., and Wilson, K. B., "On the Experimental Attainment of Optimum Conditions," *Breakthroughs in Statistics: Methodology and Distribution*, edited by S. Kotz, and N. L. Johnson, Springer, New York, 1992, pp. 270–310. https://doi.org/10.1007/978-1-4612-4380-9_23

[17] Buhmann, M. D., *Radial Basis Functions: Theory and Implementations*, Vol. 12, Cambridge Univ. Press, New York, 2003. https://doi.org/10.1017/CBO9780511543241

[18] Rosenblatt, F., "Principles of Neurodynamics. Perceptrons and the Theory of Brain Mechanisms," Cornell Aeronautical Lab., Inc. TR RTO-EN-AVT-194, Buffalo, NY, 1961.

[19] Krige, D. G., "A Statistical Approach to Some Mine Valuation and Allied Problems on the Witwatersrand," Ph.D. Thesis, Univ. of the Witwatersrand, Johannesburg, South Africa, 1951.

[20] Sobol', I., "Uniformly Distributed Sequences with Additional Uniformity Properties," *USSR Computational Mathematics and Mathematical Physics*, Vol. 16, No. 5, 1976, pp. 1332–1337. https://doi.org/10.1016/0041-5553(76)90154-3

[21] Saltelli, A., Ratto, M., Andres, T., Campolongo, F., Cariboni, J., Gatelli, D., Saisana, M., and Tarantola, S., *Global Sensitivity Analysis: The Primer*, Wiley, Hoboken, NJ, 2008, pp. 155–182, Chap. 4. https://doi.org/10.1002/9780470725184

[22] *ANSYS Electronics Desktop Suite ver.17.2 Users' Guide*, ANSYS, Inc., PA, 2016.

[23] Genovese, A., Lazurenko, A., Koch, N., Weis, S., Schirra, M., van Reijen, B., Haderspeck, J., and Holtmann, P., "Endurance Testing of HEMPT-Based Ion Propulsion Modules for SmallGEO," *Proceedings of 32nd International Electric Propulsion Conference*, Vol. 11, IEPC-2011-141, Wiesbaden, Sept. 2011, p. 15.

[24] Howard, J., "Introduction to Plasma Physics C17 Lecture Notes," 2002, people.physics.anu. edu.au/jnh112/AIIM/c17/chap04.pdf [retrieved 15 April 2018].

[25] Gallimore, A., "The Physics of Spacecraft Hall-Effect Thrusters," *61st Annual Meeting of the APS Division of Fluid Dynamics*, American Physical Society, Nov. 2008.

[26] Matlock, T. S., "An Exploration of Prominent Cusped-Field Thruster Phenomena: The Hollow Conical Plume and Anode Current Bifurcation," Ph.D. Thesis, Massachusetts Inst. of Technology, Cambridge, MA, 2012.

[27] Young, C. V., Smith, A. W., and Cappelli, M. A., "Preliminary Characterization of a Diverging Cusped Field (DCF) Thruster," *31st International Electric Propulsion Conference*, IEPC-2009-166, Ann Arbor, MI, Sept. 2009.
https://doi.org/10.13140/2.1.2644.5123

[28] Koch, N., Schirra, M., Weis, S., Lazurenko, A., van Reijen, B., Haderspeck, J., Genovese, A., Holtmann, P., Schneider, R., Matyash, K., and Kalentyev, O., "The HEMPT Concept-A Survey on Theoretical Considerations and Experimental Evidences," *Proceedings of 32nd International Electric Propulsion Conference*, Vol. 11, IEPC-2011-236, Wiesbaden, Germany, Sept. 2011, p. 15.

[29] Courtney, D. G., "Development and Characterization of a Diverging Cusped Field Thruster and a Lanthanum Hexaboride Hollow Cathode," Ph.D. Thesis, Massachusetts Inst. of Technology, Cambridge, MA, 2008.

[30] "CubeSat 101 Basic Concepts and Processes for First-Time CubeSat Developers," NASA CubeSat Launch Initiative, NP-2017-10-2470-HQ, Washington, D.C., 2017.

[31] Matyash, O. K., Schneider, R., Taccogna, F., Koch, N., and Schirra, M., "Kinetic Simulation of the Stationary HEMP Thruster Including the Near-Field Plume Region," *Proceedings of the 31st International Electric Propulsion Conference*, IEPC-2009-110, Ann Arbor, MI, Sept. 2009, pp. 20–24.

[32] Kalentev, O., Matyash, K., Duras, J., Lüskow, K. F., Schneider, R. E., Koch, N., and Schirra, M., "Electrostatic Ion Thrusters—Towards Predictive Modeling," *Contributions to Plasma Physics*, Vol. 54, No. 2, 2014, pp. 235–248.
https://doi.org/10.1002/ctpp.v54.2

[33] Kornfeld, G., Koch, N., and Coustou, G., "First Test Results of the HEMP Thruster Concept," *28th International Electric Propulsion Conference*, IEPC 2003-112, Toulouse, France, Sept. 2003.

[34] Boris, J. P., "Relativistic Plasma Simulation-Optimization of a Hybrid Code," *Proceeding of 4th Conference on Numerical Simulations of Plasmas*, edited by J. P. Boris, and R. A. Shanny, Plasma Physics Division Naval Research Lab., Nov. 1970.

[35] Tskhakaya, D., Matyash, K., Schneider, R., and Taccogna, F., "The Particle-in-Cell Method," *Contributions to Plasma Physics*, Vol. 47, Nos. 8–9, 2007, pp. 563–594.
https://doi.org/10.1002/ctpp.200710072

[36] Hayashi, M., "Bibliography of Electron and Photon Cross Sections with Atoms and Molecules Published in the 20th Century—Xenon," National Inst. for Fusion Science TR NIFS-DATA-79, Danvers, MA, 2003, http://www.nifs.ac.jp/report/NIFS-DATA-079.pdf.

[37] Komurasaki, K., Hirakawa, M., and Arakawa, Y., "Plasma Acceleration Process in a Hall-Current Thruster," *37th International Electric Propulsion Conference*, IEPC-91-078, Viareggio, Italy, Oct. 1991.

[38] Martinez-Sanchez, M., and Lozano, P., "16.522 Space Propulsion," 2015, https://ocw.mit.edu/courses/aeronautics-and-astronautics/16-522-space-propulsion-spring-2015/lecture-notes/MIT16_522S15_Lecture17.pdf [retrieved 1 July 2019].

J. T. Cassibry
Associate Editor